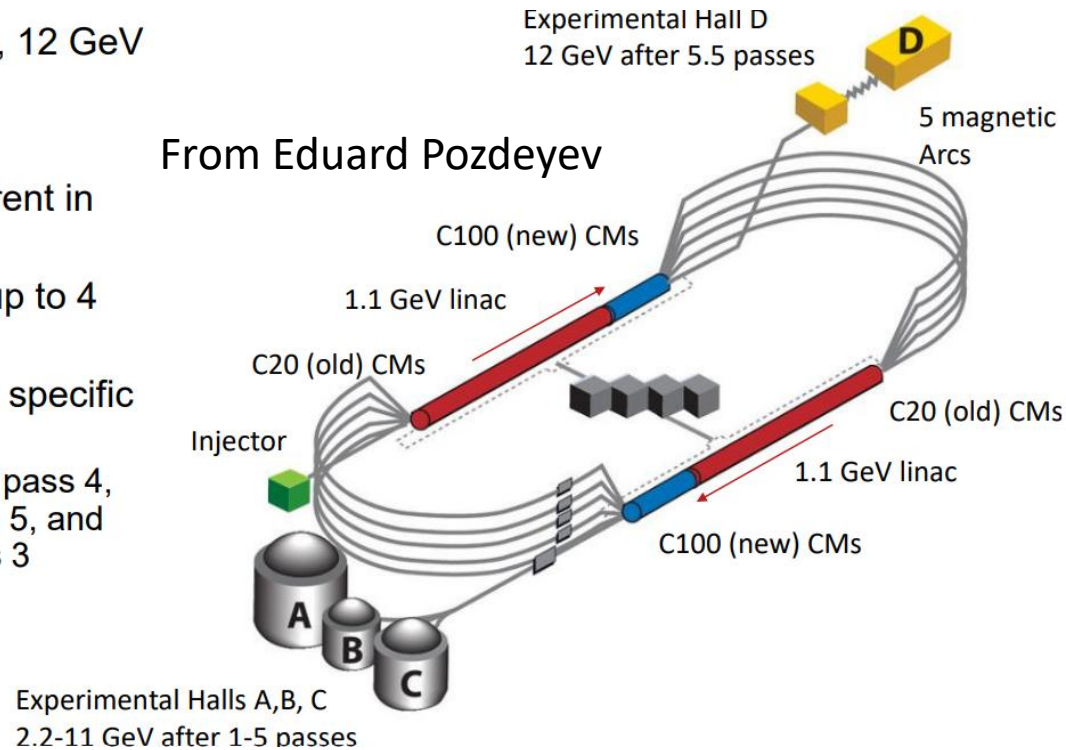


# Recent Results from Jlab

G.M. Urciuoli

# Jlab CEBAF accelerator provides an outstanding electron beam to perform an excellent hypernuclear spectroscopy

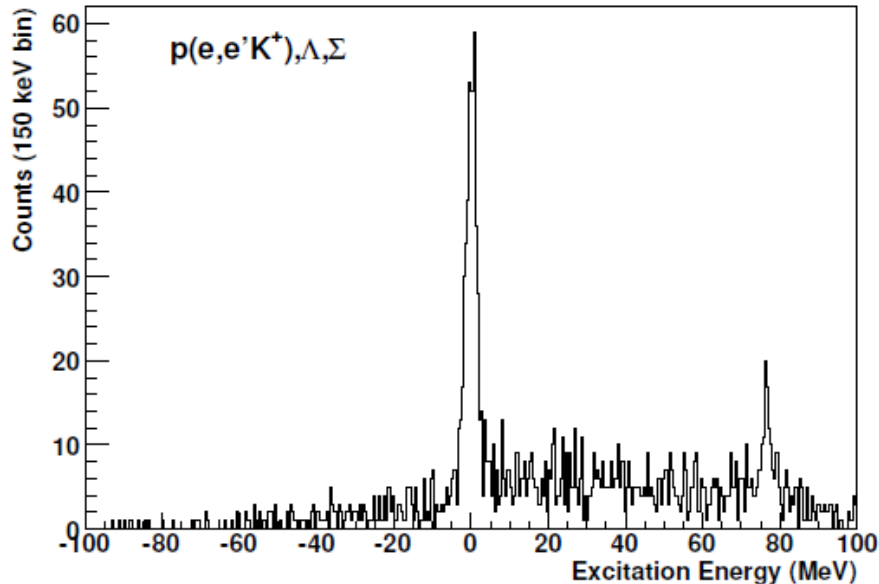
- SRF, recirculating, 5.5 pass, 12 GeV Linac
- Beam power up to 900 kW
- Total recirculated beam current in the linac up to 450  $\mu\text{A}$
- CEBAF can provide beam up to 4 Halls simultaneously
- Beam can be extracted to a specific Hall at any selected pass
  - e.g., Hall A can operate at pass 4, Hall B can operate at pass 5, and Hall C can operate at pass 3



Energy (hall D)	12 GeV
Energy (halls A, B, and C)	11 GeV
Average current (halls A and C)	1–90 $\mu\text{A}$
Average current (hall B)	1–100 nA
Average current (hall D)	0.1–5 $\mu\text{A}$
Bunch charge	<0.5 pC
Repetition rate	249.5 MHz/hall
Beam polarization	90%
Beam size (rms transverse)	~150 $\mu\text{m}$
Bunch length (rms)	300 fs, 90 $\mu\text{m}$
Energy spread	$2 \times 10^{-4}$

Beam power	<1 MW
Beam loss	<1 $\mu\text{A}$
Number of passes	5.5
Number of accelerating cavities	418
Fundamental mode frequency	1497 MHz
Amplitude control	$1 \times 10^{-4}$
Phase control	$0.1^\circ$ rms
Cavity operating temperature	2.1 K
Liquifier 2 K cooling power	10 kW
Liquifier operating power	10 MW

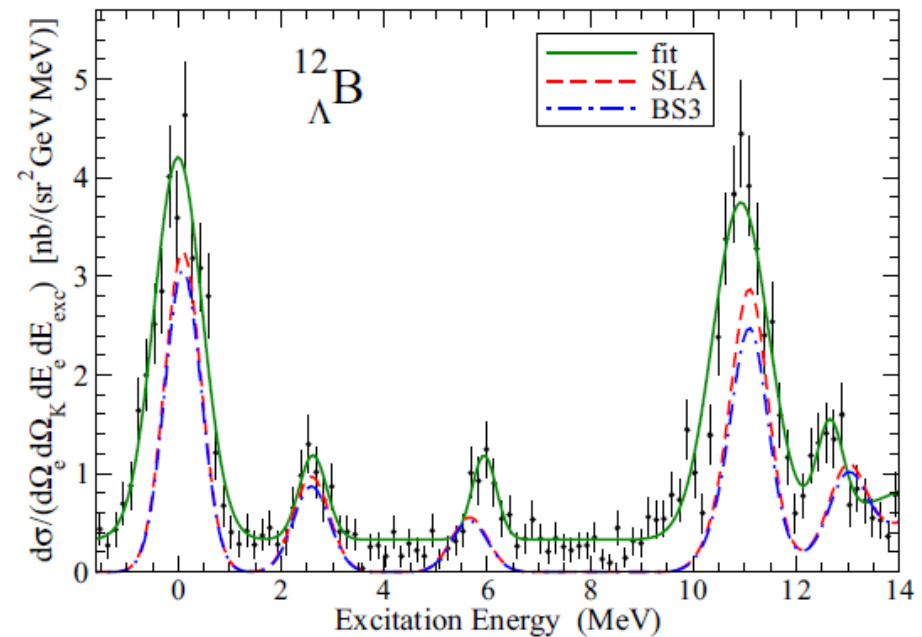
# Features of the hypernuclear spectroscopy performed through ${}^AZ(e, e'K^+){}_{\Lambda}^A(Z - 1)$ reactions:



## Energy calibration

Thanks to the availability of Hydrogen targets and hence to the possibility to determine the excitation energy spectrum of the reaction:

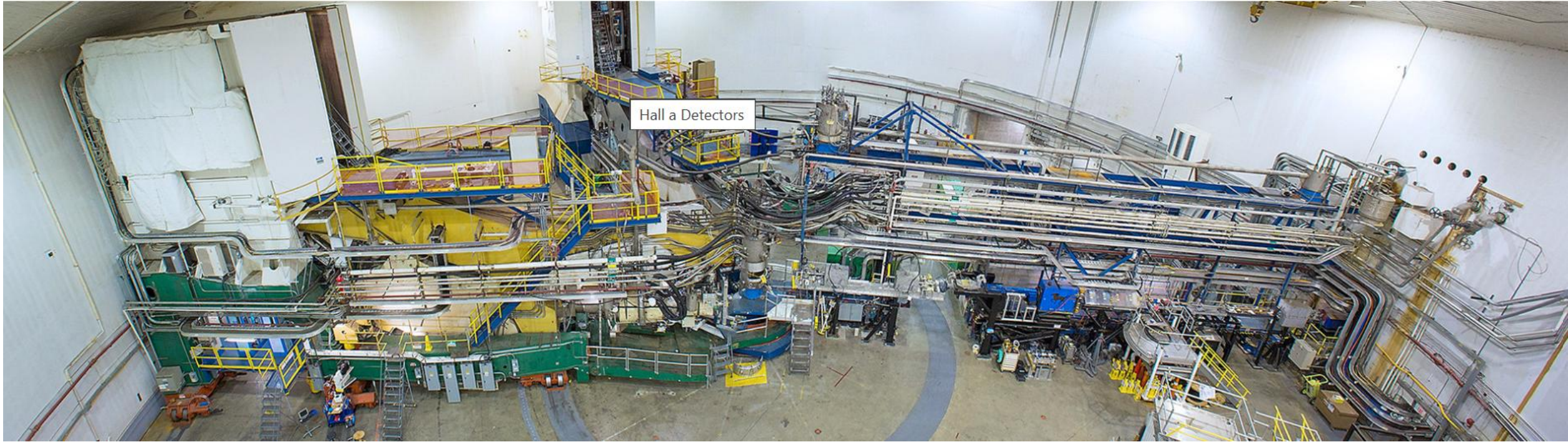
${}^1H(e, e'K^+)_{\Lambda, \Sigma}$  it is possible to obtain very good **energy calibration** and hence to determine very precisely binding energies



## Energy resolution:

thanks to high resolution spectrometers and the high monochromatic incident electron beam sub-MeV energy resolutions were obtained at Jlab

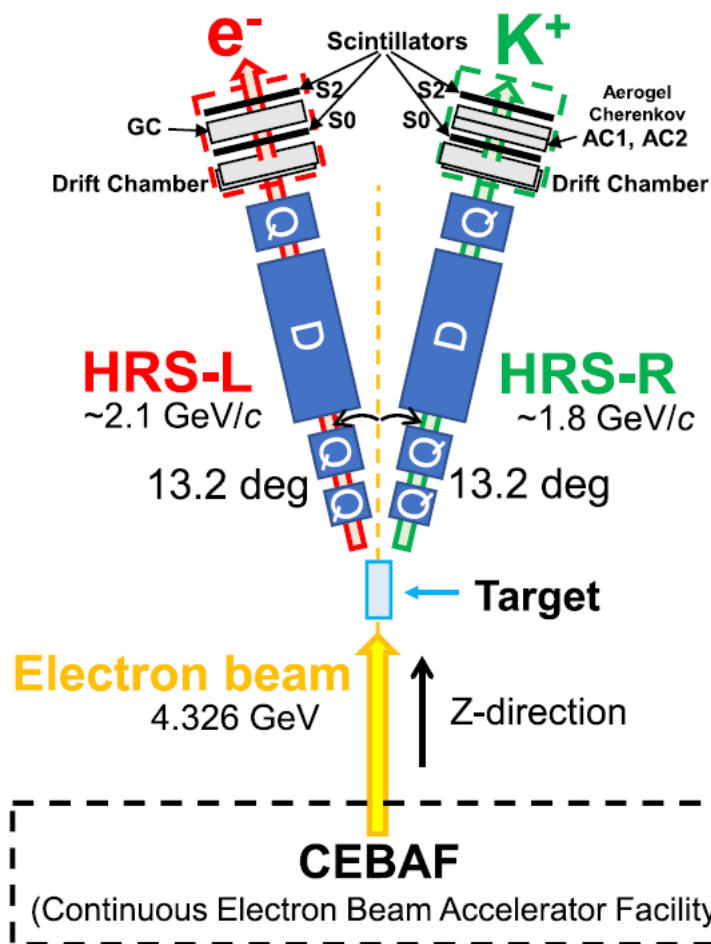




Recent hypernuclear spectroscopy was performed at Jlab in Hall A (experiment E12-17-003)

Hall A is equipped with two nearly equal High Resolution Spectrometers:  
HRS-L for the detection of the scattered electrons.  
HRS-R for the detection of the produced hadrons.

# E12-17-003 experimental setup



$$(Q^2 \simeq 0.5 \text{ (GeV/c)}^2; W = 2.14; \text{ GeV}; \theta_{c.m.}^{\gamma k} \simeq 8^\circ)$$

Parameter	Value
Electron beam ( $e$ )	
Beam energy	4.326 GeV
Energy spread ( $\Delta E/E$ in FWHM)	$\leq 1.0 \times 10^{-4}$
Scattered electron ( $e'$ )	
Central momentum	2.100 GeV/c
Momentum acceptance	4.5%
Momentum resolution ( $\Delta p/p$ in FWHM)	$1.0 \times 10^{-4}$
Kaon ( $K^+$ )	
Central momentum	1.823 GeV/c
Momentum acceptance	4.5%
Momentum resolution ( $\Delta p/p$ in FWHM)	$1.0 \times 10^{-4}$

Target	Beam Current [ $\mu\text{A}$ ]	Beam Charge [C]	$N_e$
Tritium	22.5	16.9	$1.1 \times 10^{20}$
Hydrogen	22.5	4.7	$2.9 \times 10^{19}$

Gaseous hydrogen target thickness 70.8 mg/cm<sup>2</sup>

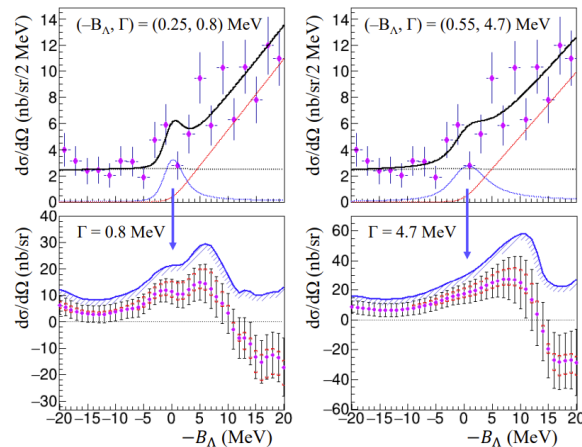
Experiment E12-17-003 primary goal was the (possible) detection of a resonance  $nn\Lambda$

Experiment E12-17-003 IN HALL A has produced two publications on this topics.

The concerned results were already presented in previous Anti-Matter, Hyper-Matter and Exotica Production Workshops

The cross-section measurement  
for the  ${}^3\text{H}(e, e'K^+)nn\Lambda$  reaction  
Prog. Theor. Exp. Phys. 2015, 00000

No significant structures were  
observed and the upper limits  
of the production-cross section  
of  $nn\Lambda$  state were obtained to  
be 21 and 31 nb/sr at the 90%  
confidence level when  
theoretical predictions of  $(-B_\Lambda, \Gamma) = (0.25, 0.8)$  and  $(0.55, 4.7)$   
MeV, respectively, were  
assumed

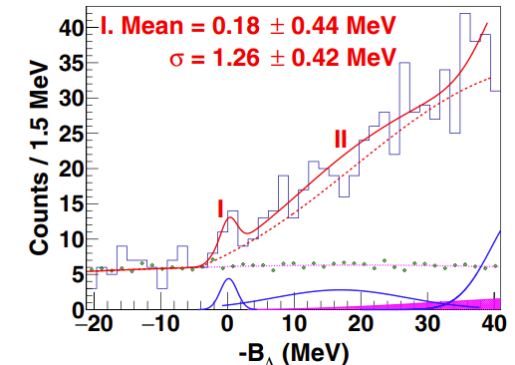


The differential cross section as a  
function of  $-B_\Lambda$  (MeV)

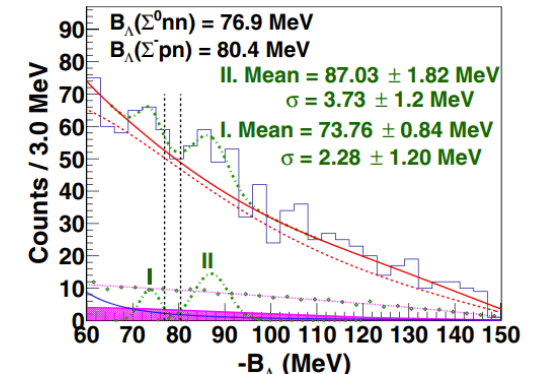
Spectroscopic study of a possible  $\Lambda nn$   
resonance and a pair of  $\Sigma NN$  states  
using the  $(e, e' K^+)$  reaction with a  
tritium target

Phys Rev. C 105, L051001(2022)

Enhancements in the missing mass  
spectrum, which may correspond to a  
possible  $\Lambda nn$  resonance and a pair  
of  $\Sigma NN$  states, were observed, although  
greater statistics are needed to make  
definitive identifications.



The enlarged mass spectrum around  
the  $\Lambda nn$  threshold.

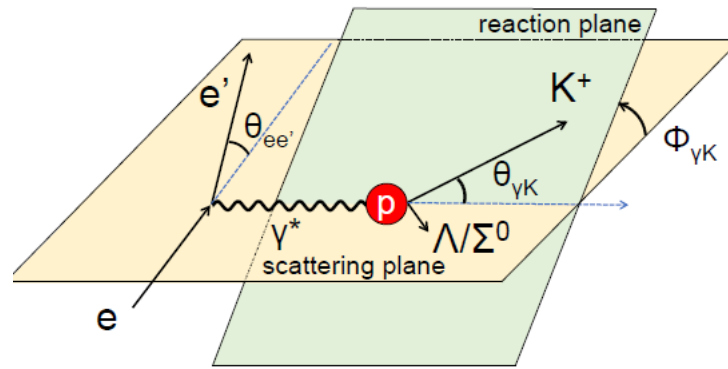


The enlarged mass spectrum at  $-B_\Lambda > 60$  MeV



# Electroproduction of the $\Lambda/\Sigma^0$ hyperons at $Q^2 \simeq 0.5 \text{ (GeV/c)}^2$ at forward angles

K. Okuyama et al. Phys. Rev. C **110**, 025203 (2024)



Determined the differential cross section for  $\Lambda/\Sigma^0$  hyperon electroproduction at forward angles, **where data are scarce**, and at a  $Q^2$  value **not well measured so far**

$$\frac{d^3\sigma}{dE_{e'} d\Omega_{e'} d\Omega_K^{c.m.}} = \Gamma \frac{d\sigma_{\gamma^*}}{d\Omega_K^{c.m.}} = \frac{d\sigma_T}{d\Omega_K^{c.m.}} + \epsilon \frac{d\sigma_{TT}}{d\Omega_K^{c.m.}} \cos 2\phi_{\gamma K} + \epsilon \frac{d\sigma_L}{d\Omega_K^{c.m.}} + \sqrt{2\epsilon(\epsilon+1)} \frac{d\sigma_{LT}}{d\Omega_K^{c.m.}} \cos \phi_{\gamma K}$$

$$\Gamma = \frac{\alpha}{2\pi Q^2} \frac{E_\gamma}{1-\epsilon} \frac{E_{e'}}{E_e} \quad \epsilon = \left[ 1 + 2 \frac{|q|^2}{Q^2} \tan^2 \left( \frac{\vartheta_{ee'}}{2} \right) \right]^{-1} \quad E_\gamma = \omega + \frac{q^2}{2m_p} \quad \omega = E_e - E_{e'} \quad q = (\omega, \mathbf{p}_e - \mathbf{p}_{e'}) \quad Q^2 = -q^2$$

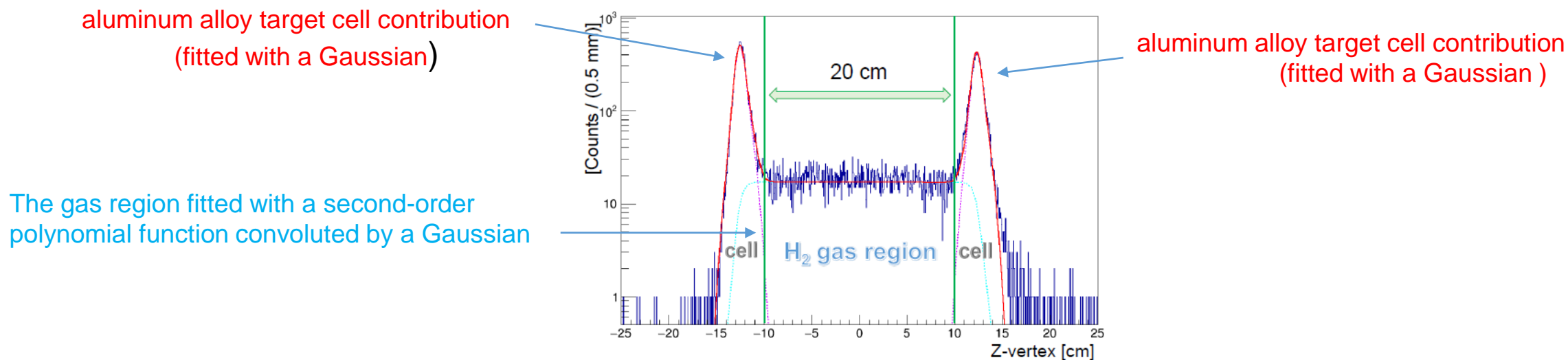
Virtual photon flux      Transverse polarization of the virtual photons      Photon equivalent energy      Virtual photon energy      4 momentum transfer

# Vertex reconstruction

HRSs bend charged particles vertically along the momentum dispersive planes.

It is possible then to reconstruct the interaction Z-vertex from the horizontal components at the focal planes because they are independent of the momentum dispersion

Z-vertex reconstruction  $\approx 5$  mm ( $1\sigma$ )



Average Z-vertex distribution obtained from the HRSs and its fitting functions (fitting range  $|Z| < 15$  cm)

Only events with  $|Z| < 10$  cm were analyzed.

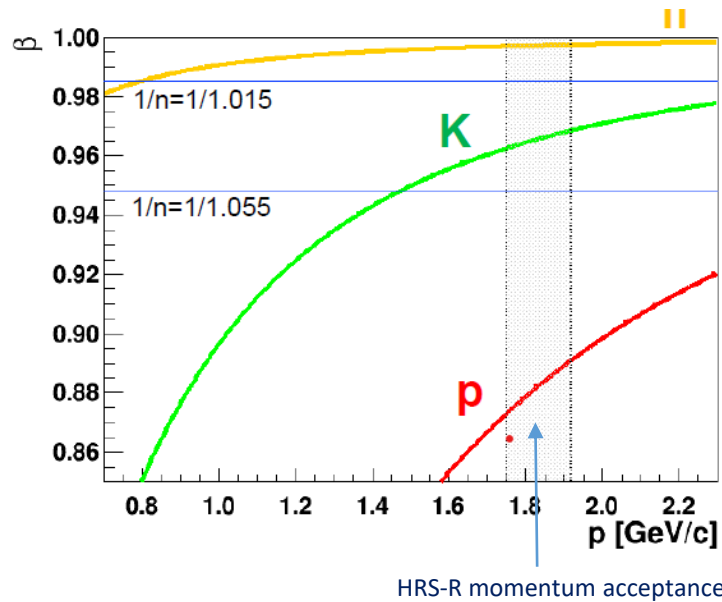
With this choice, aluminum contamination ratio was:  $0.3 \pm 0.05$  (Stat.)  $^{+0.84}_{-0.00}$  (Syst.) %

Contribution from the events outside the fitting range



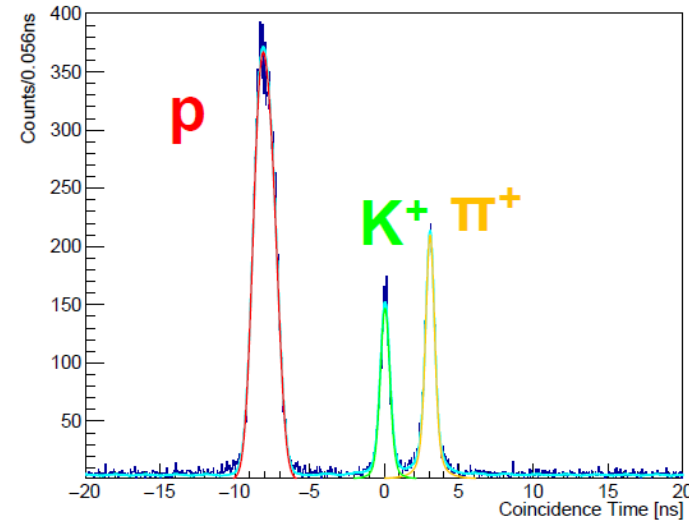
# Kaon identification

Two steps



First step:

Two Cherenkov detectors were used  
With two different refraction indexes.  
Pions fired both, Kaons only one  
and protons none of them



Second step:

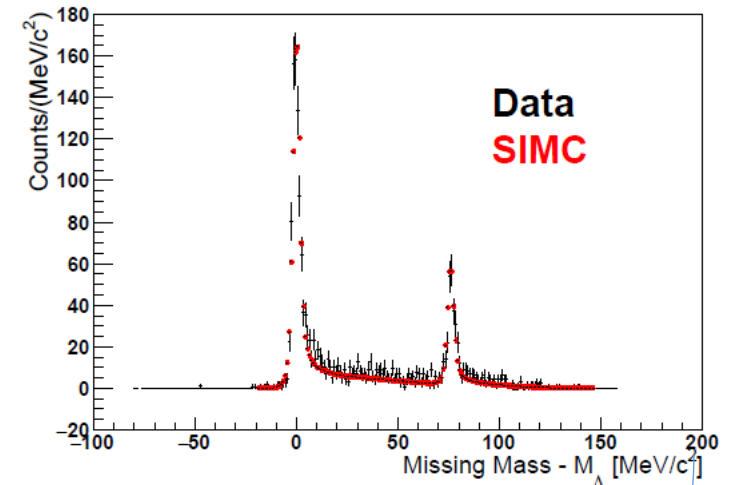
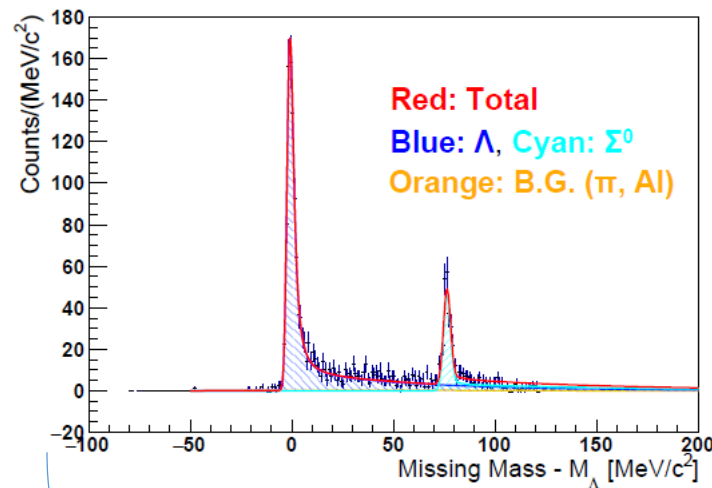
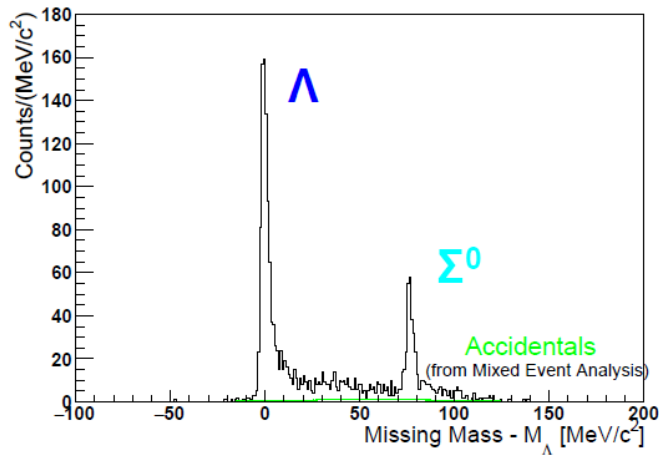
For particles firing only the  $\frac{1}{n} = \frac{1}{1.055}$  Cherenkov detector, the coincidence time, i. e., the difference between electron and hadron time-of-flight (TOF)s inside HRS-L and HRS-R respectively was measured. Calculating the hadron time-of-flight with the Kaon mass, the coincidence time is zero only for Kaons from true ( $e, e'K^+$ ) events.

Fitting the coincidence time spectrum, applying a cut on the coincidence time of  $|t_{\text{Coin.}}| < 1$  ns.

the pion contamination was evaluated as:  $1.77^{+0.32}_{-0.28}(\text{Stat.})^{+0.40}_{-0.04}(\text{Syst.})\%$

# Accidentals subtraction and radiative tails

$$M_x = \sqrt{(E_e - E_{e'} + M_p - E_k)^2 - (\mathbf{P}_e - \mathbf{P}_{e'} - \mathbf{P}_k)^2}$$



Accidentals contribution to the Missing Mass spectrum was deduced by making a distribution with artificially mixed events corresponding to random coincidences between the two HRS spectrometers.

Two techniques were used to take into account radiative corrections:

a) fitting the spectrum by using only the real data:

$(f + h) * g(x) = (f * g)(x) + (h * g)(x)$  for both  $\Lambda$  and  $\Sigma^0$  tails

$f(x)$  exponential,  $h(x)$  Landau,  $g(x)$  gaussian)

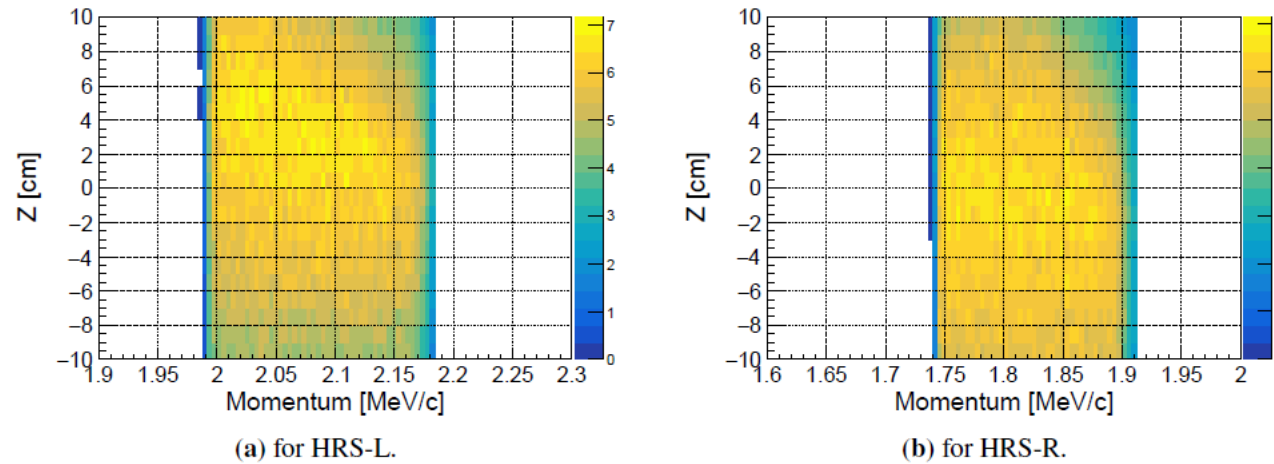
Voigts for both the pion contamination and target cell contributions

b) using a Monte-Carlo simulation (e.g. SIMC code).

Because of the possible presence of unknown background, technique

b) gives a smaller number of detected hyperons than technique a) which reproduces the real data well and whose fit was chosen as the most faithful. The variations of the fitting results by changing the fit conditions and the integral ranges, as well as those reflecting the distribution reproduced by SIMC, were taken into account as systematic errors.

# Spectrometer solid angles and virtual photon flux determination



The two-dimensional dependence of the solid angle on momentum and  $Z$ -vertex for HRS-L and HRS-R.  
The  $Z$ -axis represents the solid angle, with units of msr.

The solid angle of the HRS is estimated through the following procedure: 1) Particles are generated uniformly and randomly from the target position. The range of momentum and solid angle are set sufficiently wider than the acceptance region of the spectrometer, and the  $Z$ -vertex is distributed within the range of  $[-10 \text{ cm}, 10 \text{ cm}]$ . 2) The solid angle acceptance of the spectrometer  $\Delta\Omega_{acc}$ , is estimated using the formula:  $\Delta\Omega_{acc} = \frac{N_{acc}}{N_{gen}} \Delta\Omega_{gen}$  where  $N_{gen}$  is the total number of generated particles,  $N_{acc}$  is the number of particles that are transmitted through the spectrometer and counted as accepted events, and  $\Delta\Omega_{gen}$  is the solid angle over which particles are generated. The number of virtual photons irradiating the proton target is:  $N_{\gamma^*} = N_e \int \Gamma d\omega d\Omega_{HRS-L}$  and by simulation resulted equal to  $N_{\gamma^*} = (7.132 \pm 0.001 (stat)) \times 10^{13}$  (4.6 C on target  $\rightarrow N_e = 2.9 \times 10^{19}$ )

# Differential cross section derivation

$$\overline{\left(\frac{d\sigma_{\gamma^*p \rightarrow K^+ \Lambda(\Sigma^0)}}{d\Omega_{K^+}}\right)}_{HRS,i} = \frac{1}{N_T} \cdot \frac{1}{N_{\gamma^*}} \cdot \frac{1}{\bar{\epsilon}} \cdot \sum_{i=1}^{N_{\Lambda(\Sigma^0)}} \frac{1}{\epsilon_i^{DAQ} \cdot \epsilon_i^{Decay} \cdot \Delta\Omega_{HRS-R,i}}$$

$N_T$ : Number of target protons (= 0.0375 b<sup>-1</sup>],  $N_{\gamma^*}$ : Number of virtual photons,  $\bar{\epsilon}$ : Average event cut efficiency,  
 $\epsilon_i^{DAQ}$ : DAQ efficiency when taking i-th event (evaluated on a run by run basis (~96%),  
 $\epsilon_i^{Decay}$ : Survival ratio of K<sup>+</sup> (~14%) ,  $\Delta\Omega_{HRS-R,i}$ : HRS-R solid angle for the i-th event (~5.5 sr)

Item	$\Lambda$		$\Sigma^0$	
	Lower	Upper	Lower	Upper
B.G. from Al Cell	0.89%	0.05%	0.89%	0.05%
Pion Contamination	0.72%	0.32%	0.72%	0.32%
Radiative tail	9.43%	4.30%	25.2%	47.6%
Kaon Survival Ratio	4.13%	0.76%	4.13%	0.76%
Number of Target Centers	0.83%	0.83%	0.83%	0.83%
Number of Beam Particles	1.00%	1.00%	1.00%	1.00%
Number of Virtual Photons	1.40%	2.30%	1.76%	1.11%
Mixed Event Analysis	0.20%	0.20%	0.30%	0.30%
All	10.53%	5.11%	25.7%	47.6%

Item	$\bar{\epsilon}(\Lambda)$ [%]	$\bar{\epsilon}(\Sigma^0)$ [%]	Description
$\epsilon^Z$	82.5	76.2	Z-vertex cut for hydrogen target selection
$\epsilon^{AC}$	60.2	59.1	Aerogel Cherenkov cut for kaon identification
$\epsilon^{CT}$	98.8	97.0	Coincidence Time cut for kaon identification
$\epsilon^{Single}$	97.0	97.0	Percentage of single-hit events in HRS-L (excluding multi-hit)
$\epsilon^{FP}$	96.2	96.2	Focal Plane cut for removing unphysical events
$\epsilon^{Track}$	98.1	98.1	Percentage of successful track reconstructions
$\epsilon^{\chi^2}$	> 99.9	> 99.9	$\chi^2$ cut for the reconstructed tracks
$\epsilon^{Total}$	44.9	40.0	Total efficiencies of the above

Efficiencies

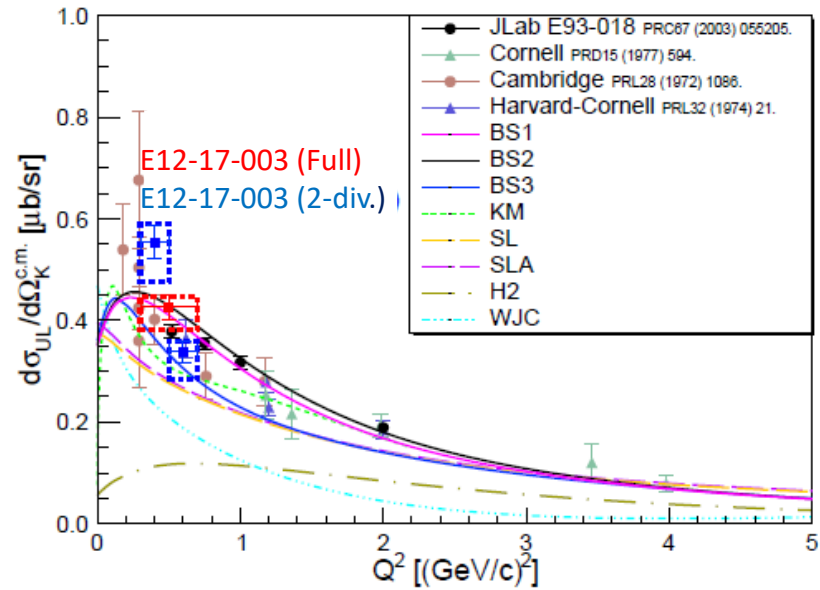
Estimated systematic errors on the differential Cross sections



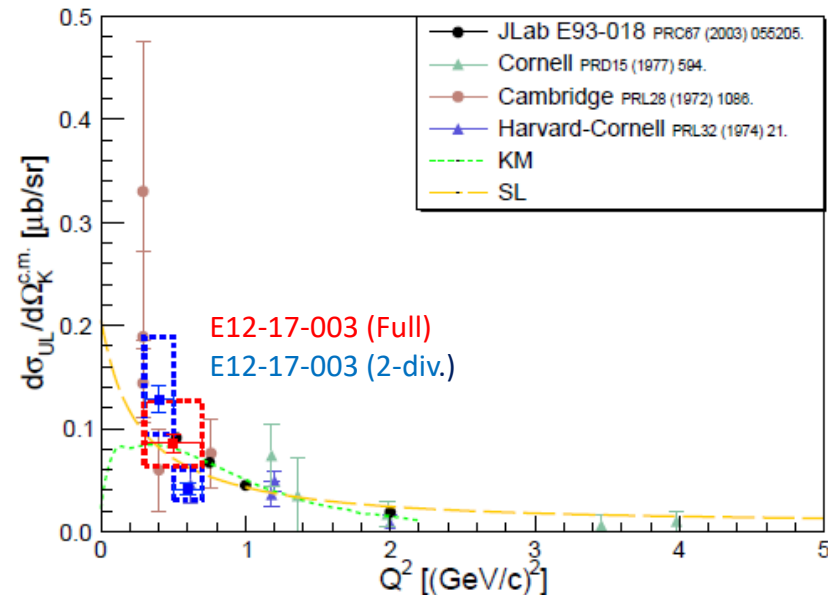
# Results

$\gamma^* p \rightarrow K^+ \Lambda$			
Full	$0.426^{+0.024}_{-0.023}(\text{Stat.})^{+0.022}_{-0.045}(\text{Syst.})$	$\mu\text{b/sr}$	at $Q^2 = 0.2 - 0.8$ $(\text{GeV}/c)^2$
Divided-1	$0.554^{+0.033}_{-0.032}(\text{Stat.})^{+0.035}_{-0.079}(\text{Syst.})$	$\mu\text{b/sr}$	at $Q^2 = 0.2 - 0.5$ $(\text{GeV}/c)^2$
Divided-2	$0.338 \pm 0.022(\text{Stat.})^{+0.022}_{-0.055}(\text{Syst.})$	$\mu\text{b/sr}$	at $Q^2 = 0.5 - 0.8$ $(\text{GeV}/c)^2$
$\gamma^* p \rightarrow K^+ \Sigma^0$			
Full	$0.086^{+0.009}_{-0.008}(\text{Stat.})^{+0.041}_{-0.022}(\text{Syst.})$	$\mu\text{b/sr}$	at $Q^2 = 0.2 - 0.8$ $(\text{GeV}/c)^2$
Divided-1	$0.128 \pm 0.013(\text{Stat.})^{+0.061}_{-0.033}(\text{Syst.})$	$\mu\text{b/sr}$	at $Q^2 = 0.2 - 0.5$ $(\text{GeV}/c)^2$
Divided-2	$0.041 \pm 0.006(\text{Stat.})^{+0.020}_{-0.010}(\text{Syst.})$	$\mu\text{b/sr}$	at $Q^2 = 0.5 - 0.8$ $(\text{GeV}/c)^2$

## Summary of the obtained differential cross sections



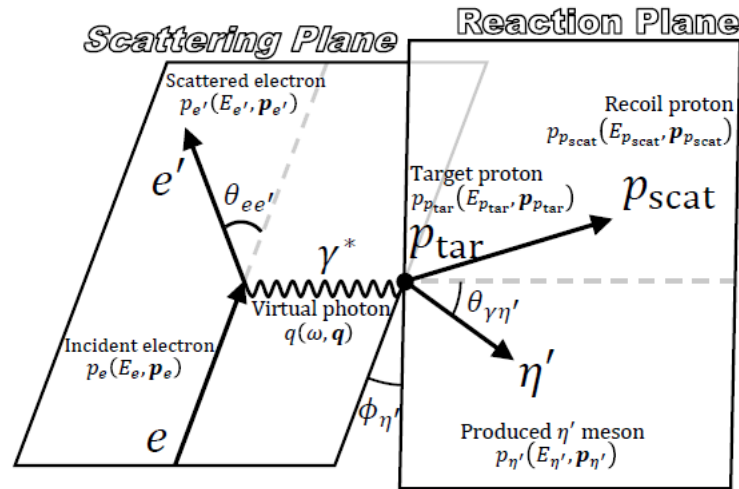
$Q^2$ -dependence of the  $p(\gamma^*, K^+)\Lambda$  differential cross section



$Q^2$ -dependence of the  $p(\gamma^*, K^+)\Sigma^0$  differential cross section

# Backward-angle electroproduction of $\eta'$ mesons off protons at $W = 2.13$ GeV and $Q^2 = 0.46$ (GeV/c)<sup>2</sup>

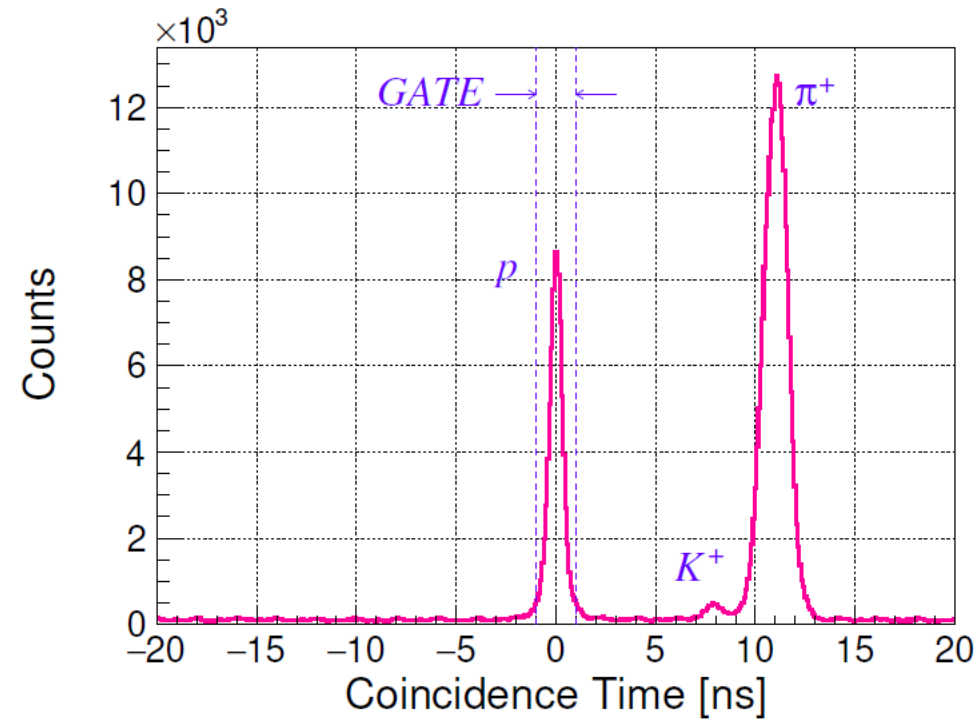
(T. Akiyama et al., **being submitted to Prog. Theor. Exp. Phys.**)



$$\frac{d^3\sigma}{dE_{e'}d\Omega_{e'}d\Omega_{\eta'}^{c.m.}} = \Gamma \frac{d\sigma_{\gamma^*}}{d\Omega_{\eta'}^{c.m.}} = \frac{d\sigma_T}{d\Omega_{\eta'}^{c.m.}} + \epsilon \frac{d\sigma_{TT}}{d\Omega_{\eta'}^{c.m.}} \cos 2\phi_{\gamma K} + \epsilon \frac{d\sigma_L}{d\Omega_{\eta'}^{c.m.}} + \sqrt{2\epsilon(\epsilon+1)} \frac{d\sigma_{LT}}{d\Omega_{\eta'}^{c.m.}} \cos \phi_{\gamma K}$$

$$\vartheta_{\gamma\eta'}^{CM} = 169^\circ; \quad \varphi_{\gamma\eta'}^{CM} = [-90^\circ, 90^\circ]; \quad \frac{\left(\frac{d\sigma}{d\Omega}\right)_{CM}}{\left(\frac{d\sigma}{d\Omega}\right)_{Lab}} = 0.0679$$

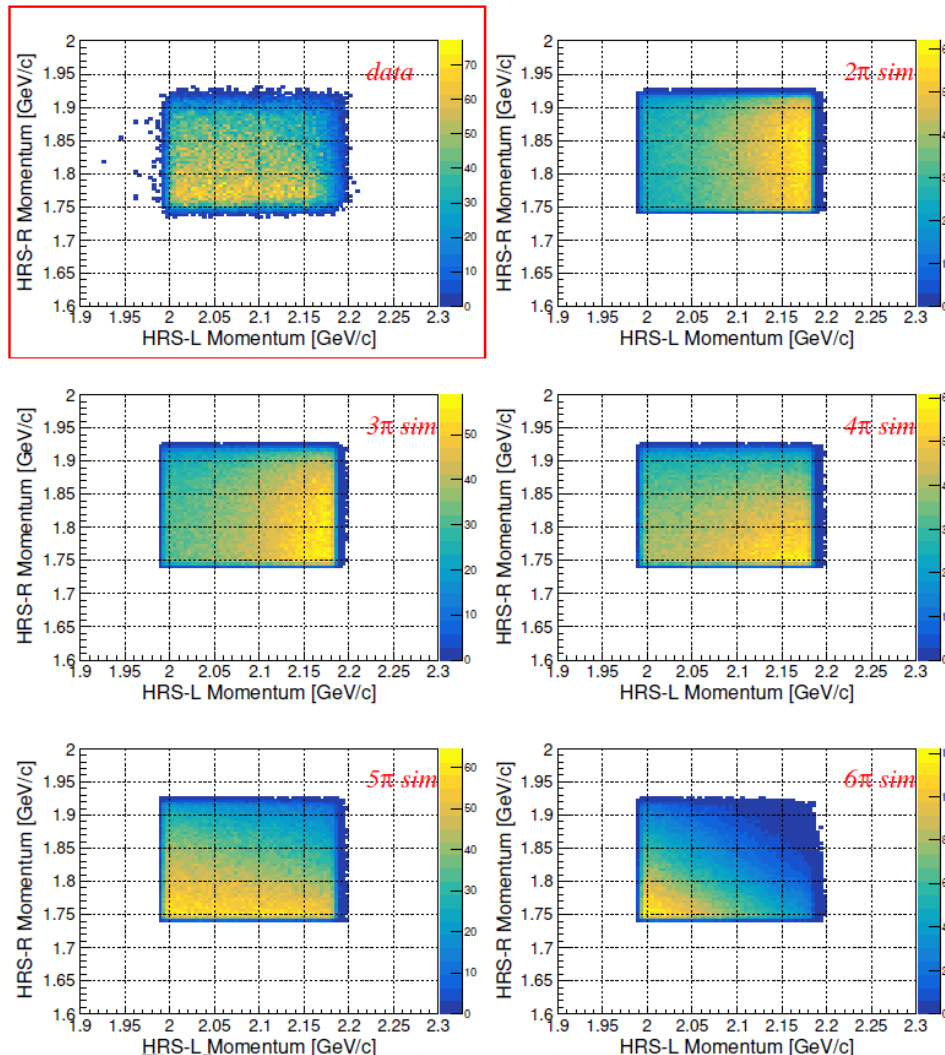
# Proton identification



Coincidence time distribution. The peaks located at 0 ns,  $\sim 7.8$  ns,  $\sim 11.1$  ns correspond to proton, kaon, and pion, respectively.

Accidental coincidence events are distributed uniformly beneath the three peaks. The two blue dashed-lines represent the timing gate for proton selection.

# Background determination



It was assumed that the background arises from multi-pion production and can be described as a superposition of events following the kinematics of non-resonant  $2\pi$ – $6\pi$  production. Distributions of  $p_{e'}$  vs  $p_p$  obtained from the multi-pion production simulation, were checked against the distribution obtained from the experimental data. Each simulated distribution was scaled so that the number of events within the acceptance matches that of the experimental data. The multiplicities of various pion production channels were linearly combined. The  $\chi^2$  value defined as:

$$\chi^2 = \sum_{i:xbins} \sum_{j:ybins} \frac{(N_{i,j}^{data} - N_{i,j}^{sim})^2}{\sigma_{i,j}^2}$$

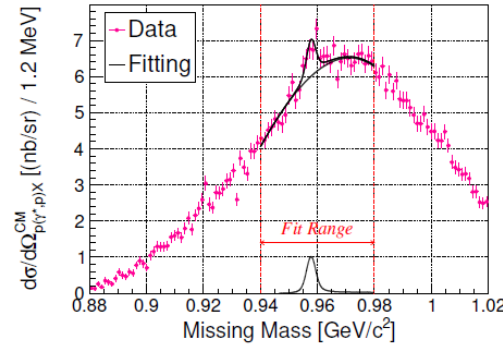
was evaluated. The set of weighting parameters that best reproduces the experimental data we determined as the one that minimized the  $\chi^2$ . The result indicates that, without applying any selections on  $Q^2$  or  $W$  the 5-pion production channel is contributing 95.5 % and the most dominant, while contributions from other channels were found to be negligibly small. The average pion multiplicity was 4.86. By mapping the simulated events onto the missing mass axis, the functional form to be used in fitting the missing mass spectrum was determined

$p_{e'}$  vs  $p_p$  distribution for data and multi-pion simulation.

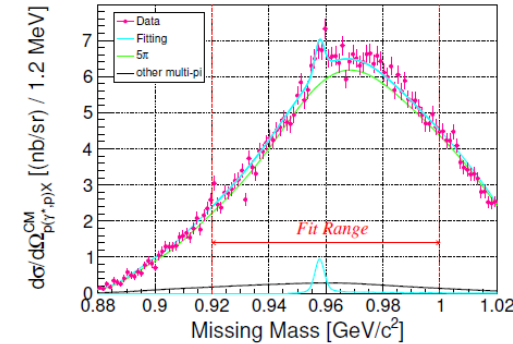


# Missing mass spectrum and $\eta'$ peak fit

$$m_X = \sqrt{\{(E_e - E_{e'}) + m_p - E_{p_{\text{scat}}}\}^2 - \{(p_e - p_{e'}) - p_{p_{\text{scat}}}\}^2}.$$



(a) Using a polynomial function for background.



(b) Using a simulation-based function for background.

Missing mass spectrum (in differential cross section) of all data with different types of fitting functions for background.

The peak shape features a tail on the higher-mass side due to electron bremsstrahlung occurring in interactions with the aluminum walls of the target cell. The missing mass distribution was then fitted with a function composed of a superposition of two Gaussian functions sharing the same peak position, and an exponentially attenuating function smeared by those Gaussians:

$$F^{\text{peak}}(x) = F^{\text{DG}}(x) + \int_{-\infty}^{+\infty} F^{\text{DG}}(x-t) F^{\text{att}}(t) dt; \quad F^{\text{DG}}(x) = A(1-C) \left[ R e^{-\frac{(x-\mu)^2}{2\sigma_1^2}} + (1-R) e^{-\frac{(x-\mu')^2}{2\sigma_1'^2}} \right]; \quad F^{\text{att}}(x) = \begin{cases} 0 & (x < \mu + \mu') \\ AC\tau e^{-\frac{x-(\mu+\mu')}{\tau}} & (\mu + \mu' \leq x) \end{cases}$$

the reduced  $\chi^2$  values between the fit function and data were 1.07 for panel (6a) and 1.49 for (6b). The difference in the cross section obtained from the two fits was 11 %, which was incorporated as a systematic error due to the fitting method. The next largest contribution to systematic error came from the uncertainty in estimating the spectrometer's solid angle. By varying the momentum range used for analysis and recalculating the cross section, this uncertainty was evaluated to be 6 %.

# Results

(Preliminary)

$$\left(\frac{d\sigma_{\gamma^*p \rightarrow Xp}}{d\Omega_p}\right)^{CM} = \frac{1}{N_{\text{Target}}} \cdot \frac{1}{\varepsilon} \sum_{i=1}^{N_{\text{Event}}} \frac{f^{\text{Lab} \rightarrow \text{CM}}}{N_{\gamma^*}(p_{e'}, z) \cdot \varepsilon_i^{\text{DAQ}} \cdot \Delta\Omega_{\text{HRS-R}}(p_p, z)}$$

$$\varepsilon = \varepsilon^Z \cdot \varepsilon^{\text{CT}} \cdot \varepsilon^{\text{RP}} \cdot \varepsilon^{\text{Single}} \cdot \varepsilon^{\text{Track}} \cdot \varepsilon^{\text{Abs}} \cdot \varepsilon^{\text{Detector}}.$$

Parameter	Explanation	Value
$\varepsilon^Z$	Efficiency for Z-vertex cut	0.630
$\varepsilon^{\text{CT}}$	Efficiency for coincidence time cut	0.936
$\varepsilon^{\text{RP}}$	Efficiency for hit position&angle cut at reference plane	0.886
$\varepsilon^{\text{Single}}$	Efficiency for selection of single-track event	0.970
$\varepsilon^{\text{Track}}$	Tracking Efficiency in VDCs	0.981
$\varepsilon^{\text{Abs}}$	Particle's loss by absorption in target	0.994
$\varepsilon^{\text{Detector}}$	Detection efficiency in hodoscopes	> 0.999
$\varepsilon^{\text{DAQ}}$	DAQ efficiency	0.96 (average)

$$\left(\frac{d\sigma_{\gamma^*p \rightarrow \eta'p}}{d\Omega_{\eta'}}\right)^{CM} = 4.4 \pm 0.8 \text{ (stat.)} \pm 0.4 \text{ (syst.) [nb/sr]}$$

$$\left(\frac{d\sigma_{\gamma^*p \rightarrow \eta'p}}{d\Omega_{\eta'}}\right)^{CM} (Q^2 < 0.47 \text{ (GeV/c}^2\text{)}) = 5.9 \pm 1.1 \text{ (stat.)} \pm 0.6 \text{ (syst.) [nb/sr]}$$

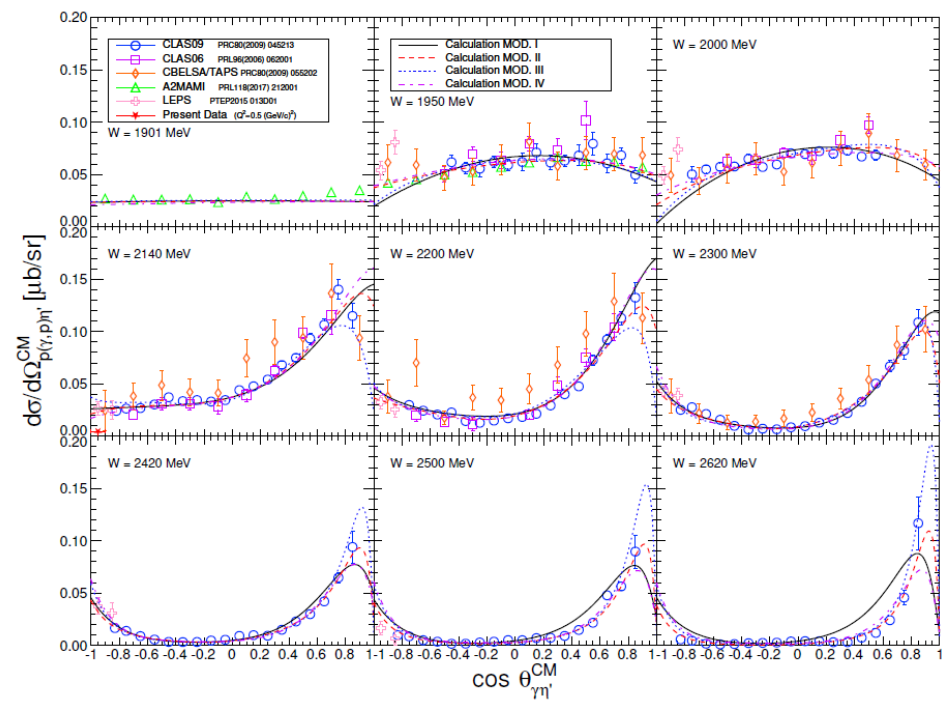
$$\left(\frac{d\sigma_{\gamma^*p \rightarrow \eta'p}}{d\Omega_{\eta'}}\right)^{CM} (Q^2 \geq 0.47 \text{ (GeV/c}^2\text{)}) = 4.3 \pm 1.1 \text{ (stat.)} \pm 0.6 \text{ (syst.) [nb/sr]}$$

$$\left(\frac{d\sigma_{\gamma^*p \rightarrow \eta'p}}{d\Omega_{\eta'}}\right)^{CM} (W < 2.13 \text{ GeV}) = 3.7 \pm 1.2 \text{ (stat.)} \pm 0.7 \text{ (syst.) [nb/sr]}$$

$$\left(\frac{d\sigma_{\gamma^*p \rightarrow \eta'p}}{d\Omega_{\eta'}}\right)^{CM} (W \geq 2.13 \text{ GeV}) = 6.5 \pm 1.0 \text{ (stat.)} \pm 0.8 \text{ (syst.) [nb/sr]}$$

# Comparison with data from other experiments and with theoretical models (1)

(Preliminary)



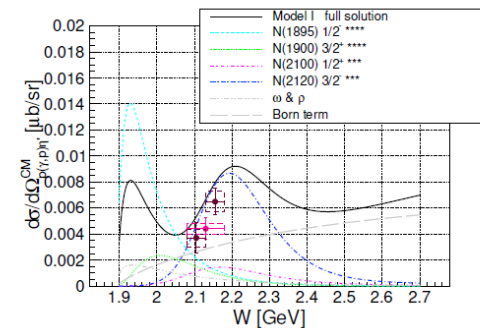
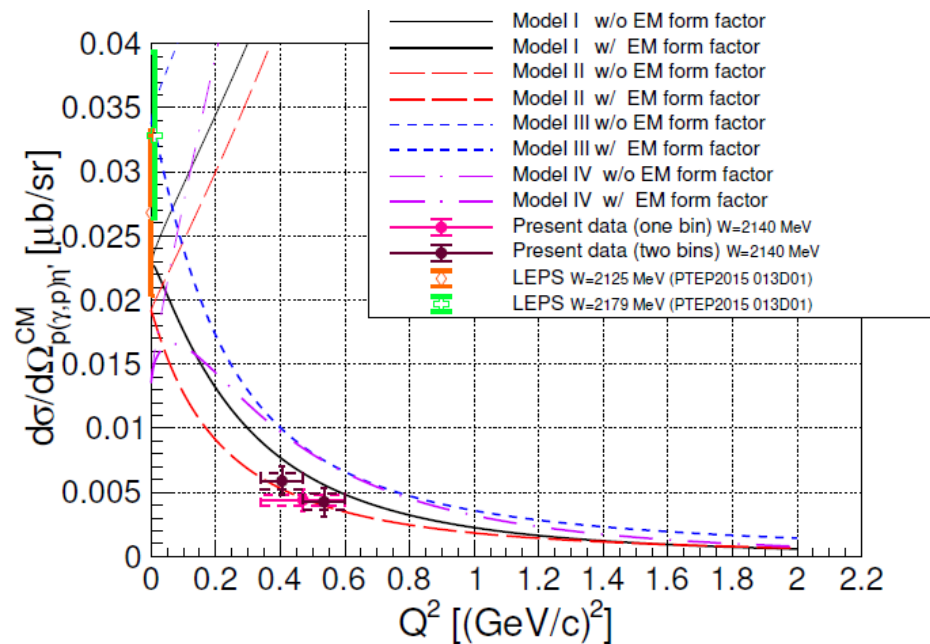
Angular dependence of  $\eta'$  photoproduction with various energy range. Plots with different colors corresponds to data by different experiment including CLAS06, CLAS09, CBELSA/TAPS, A2MAMI and LEPS. A red star with error bars represents the result of the present result at  $W = 2140$  MeV and  $\cos\theta_{\gamma\eta'}^{CM} \approx -1$ . Smooth curves give the solution of Model I–IV.

Resonance	PDG status	Model I	Model II	Model III	Model IV
$\rho$ (770)		✓	✓	✓	✓
$\omega$ (782)		✓	✓	✓	✓
$N$ (1860) $5/2^-$	**			✓	
$N$ (1875) $3/2^-$	***				✓
$N$ (1880) $1/2^+$	***		✓	✓	
$N$ (1895) $1/2^-$	****	✓	✓	✓	◊
$N$ (1900) $3/2^+$	****	✓	✓	✓	◊
$N$ (2000) $5/2^+$	**			✓	
$N$ (2060) $5/2^-$	***		✓		
$N$ (2100) $1/2^+$	***	✓	✓		✓
$N$ (2120) $3/2^-$	***	✓	✓	✓	✓

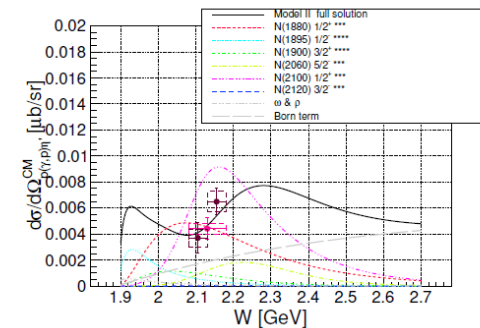
Summary of resonance sets incorporated into the isobar model calculation Model I–IV. All three models have  $\rho$  (770) and  $\omega$  (782) meson coupling in  $t$ -channel. The diamond symbols  $\diamond$  indicates that the mass and width have been slightly modified from the PDG summary values

# Comparison with data from other experiments and with theoretical models (2)

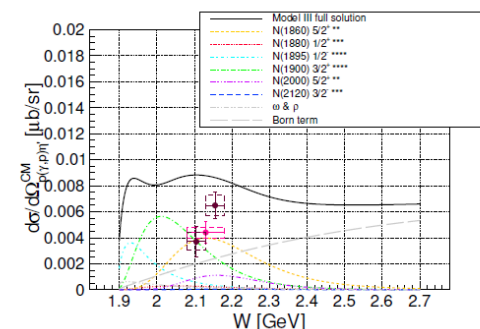
(Preliminary)



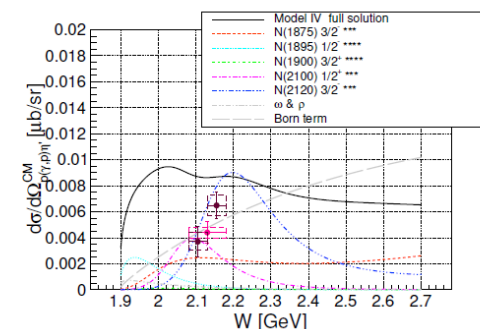
(a) Compared with Model I.



(b) Compared with Model II.



(c) Compared with Model III.



(d) Compared with Model IV.

$Q^2$ -dependence of the differential cross section in electroproduction of the  $\eta'$ . Bold/thin curves correspond to calculation with/without the electromagnetic form factor. The pink plot with errors represents the result of the present experiment in a single bin. In contrast, the brown plots are the results divided into two bins. The error bars to each plot represent statistical errors, while the boxes represent systematic errors. The green and orange plots at  $Q^2 = 0$  (overlapping each other) are the value of existing data at nearby  $W$  of photoproduction measured by LEPS

$W$ -dependence of the differential cross section of the  $\eta'$  electroproduction. The pink plot with errors represents the result of the present experiment in a single bin. In contrast, The brown plots are the results divided into two bins. The error bars to each plot represent statistical errors, while the boxes represent systematic errors. The solid curves give the full solutions of Model I–IV at the specific kinematics, and the other curves give the individual contributions of different resonances.



# The future:

## Hall C - Hypernuclei

Three are the goals of the present hypernuclear program at JLab:

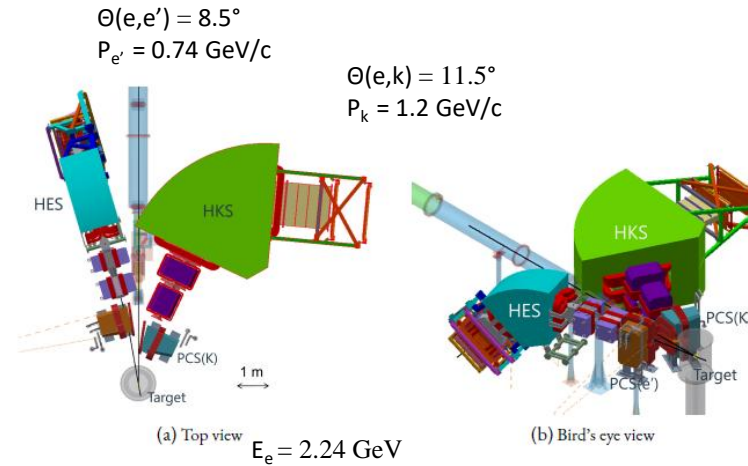
- Neutron star structure investigation (solution of the “hyperon puzzle”)
- Charge symmetry breaking study in hyperon – nucleon interaction
- Study of nucleus deformations

Despite this program address different topics, the experimental method to achieve all the aforementioned goals is the same: hypernuclear spectroscopy that has to be performed with the best achievable energy resolution and the best achievable binding energy measurement precision.

Because of that, all the experiments that are being proposed to achieve the Jlab hypernuclear program goals will employ the same identical experimental apparatus (but the target).

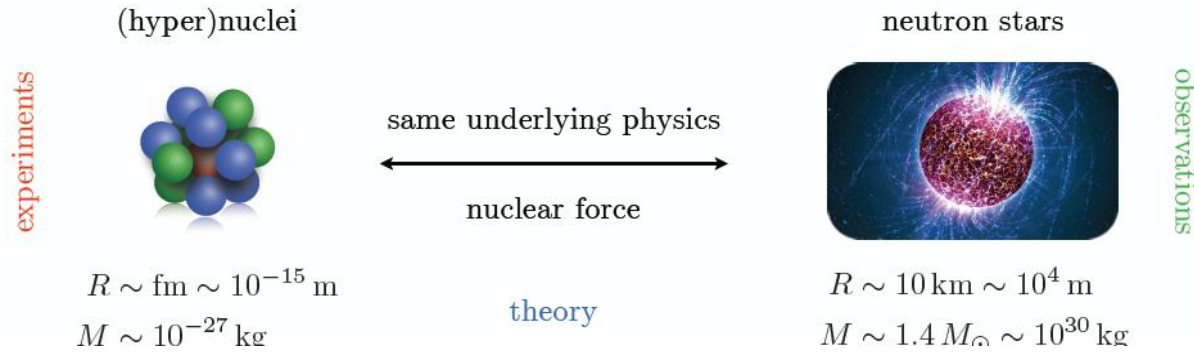
# The experimental apparatus:

The new Experimental setup and kinematics after moving in Hall C



Item		Value
Beam ( $e$ )	Energy (/GeV)	2.24
	(Required) energy spread and drift	$1 \times 10^{-4}$ (FWHM)
PCS + HES ( $e'$ )	Central momentum $p_{e'}^{\text{cent.}}$ [/(GeV/c)]	0.74
	Central angle $\theta_{e'}^{\text{cent.}}$	$8.5^\circ$
	Solid angle acceptance $\Omega_{e'}$ (/msr) (at $p_{e'}^{\text{cent.}}$ )	3.4
	Momentum resolution $\Delta p_{e'}/p_{e'}$	$4.4 \times 10^{-4}$ (FWHM)
PCS + HKS ( $K^+$ )	Central momentum $p_{K^+}^{\text{cent.}}$ [/(GeV/c)]	1.20
	Central angle $\theta_{eK^+}^{\text{cent.}}$	$11.5^\circ$
	Solid angle acceptance $\Omega_{K^+}$ (/msr) (at $p_{K^+}^{\text{cent.}}$ )	7.0
	Momentum resolution $\Delta p_{K^+}/p_{K^+}$	$2.9 \times 10^{-4}$ (FWHM)
$p(e, e'K^+)\Lambda$	$\sqrt{s} = W$ (/GeV)	1.912
	$Q^2$ [/(GeV/c) $^2$ ]	0.036
	$K^+$ scattering angle wrt virtual photon, $\theta_{\gamma^*K^+}$	$7.35^\circ$
	$\epsilon$	0.59
	$\epsilon_L$	0.0096

# Neutron star structure

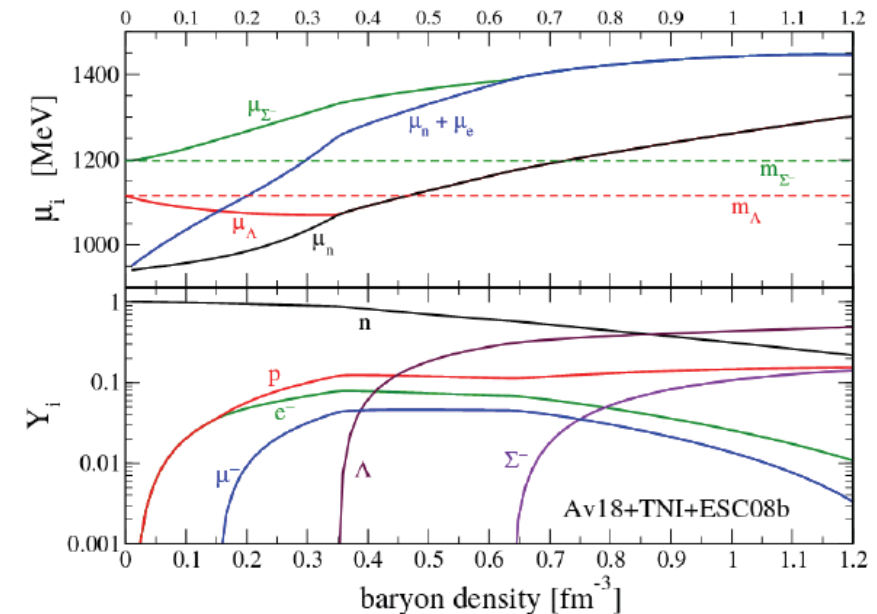


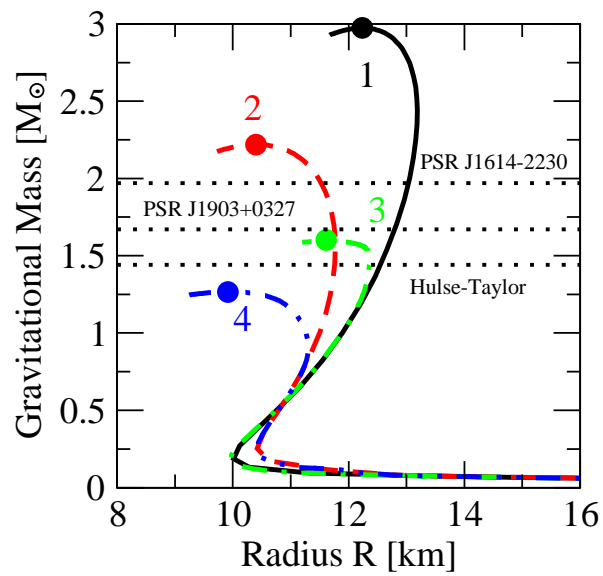
Hyperons are expected to appear in their core at  $r \sim (2-3)r_0$  when  $m_N$  is large enough to make conversion of N to Y energetically favorable.

However, this results in a reduction of the Fermi pressure exerted by the baryons and a softening of the equation of state (EOS). As a consequence, the maximum mass determined by the equilibrium condition between gravitational and nuclear forces is reduced.

Most of EOS of matter containing strangeness predict a maximum neutron star mass of about 1.5 solar masses. However, the recent measurements of neutron star masses as big as 2 solar masses require a much stiffer EOS (Hyperon puzzle).

Neutron stars are remnants of the gravitational collapse of massive stars having masses of (1-2 solar masses  $\sim 2 \times 10^{33} \text{ Kg}$ ) and are excellent observatories to test fundamental properties of nuclear matter under extreme conditions and offer interesting interplay between nuclear processes and astrophysical observables

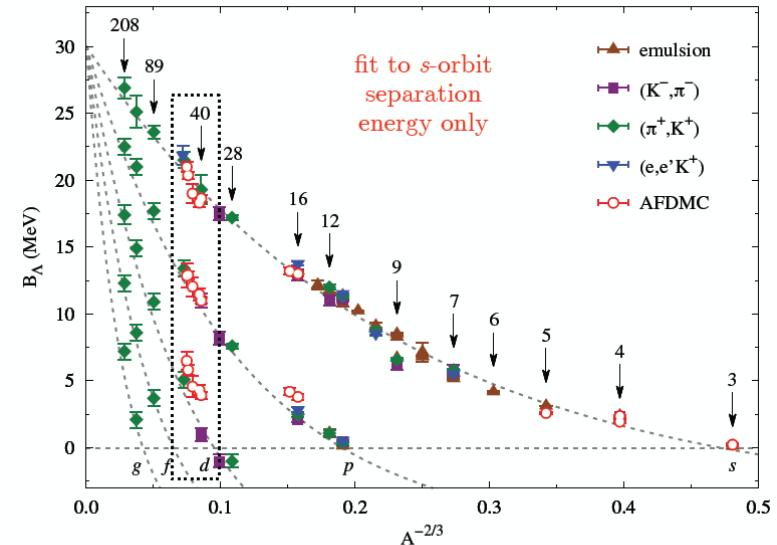
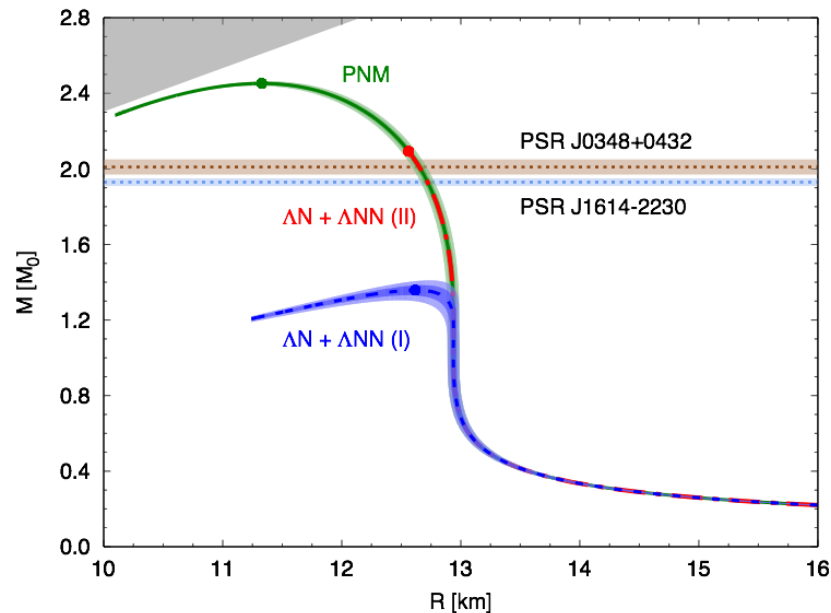




It clearly appears that the inclusion of YNN forces (curve 3) leads to a large increase of the maximum mass, although the resulting value is still below the two solar mass line.

1. Nucleons without 3 body forces
2. Nucleons with 3 body forces
3.  $\Lambda$  and N with 3 body forces ( $\Lambda$ NN)
4.  $\Lambda$  and N without 3 body force

D.Lonardon et al., Phys. Rev. Lett. 114, 092301 (2015) (AFDMC)



# Two proposals to solve the “hyperon puzzle”

## Experiment E12-24-013

An isospin dependence study of the Lambda-N interaction through the high precision spectroscopy of Lambda hypernuclei with electron beam.

Neutron stars are 90% made up of neutrons. The effect of asymmetry of the nuclear medium on the hyperon chemical potential can be translated into an isospin dependence of YNN interaction. Very accurate measurements of asymmetric hypernuclei binding energies are hence necessary. According to Auxiliary-Field Diffusion Monte Carlo (AFMC) calculations, if the three-body  $\Lambda$ NN repulsive force has isospin dependence it would result in a shift in the energy dependence when the neutron-rich  ${}^{48}_{\Lambda}K$  target is used. On the other hand the effect of isospin dependence is small for the target  ${}^{40}_{\Lambda}K$  with equal numbers of protons and neutrons.

## Experiment E12-24-003

Studying  $\Lambda$  interactions in nuclear matter with the  ${}^{208}Pb(e, e'K^+){}^{208}_{\Lambda}Tl$  reaction

The measured charge density distribution of  ${}^{208}Pb$  clearly shows that the region of nearly constant density accounts for a very large fraction (~70 %) of the nuclear volume, thus suggesting that its properties largely reflect those of uniform nuclear matter in the neutron star

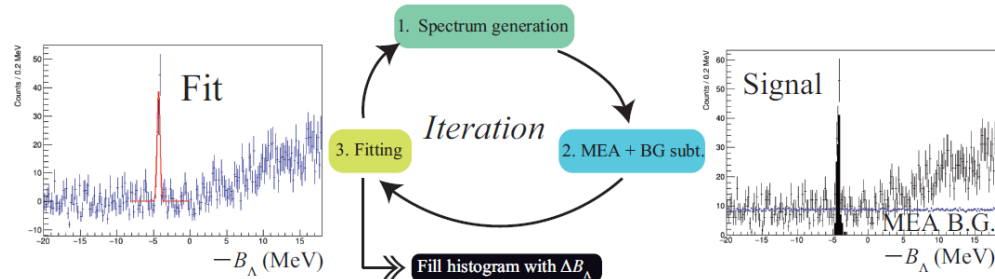
The validity of this conjecture has been long established by a comparison between the results of theoretical calculations and the data extracted from the  ${}^{208}Pb(e, e'p){}^{207}Tl$  cross sections measured at NIKHEF in the 1990s



# Charge symmetry breaking (Experiment E12-24-004)

## Study of Charge Symmetry Breaking in p-shell hypernuclei



${}^6_\Lambda\text{He}$ ,  ${}^9_\Lambda\text{Li}$ , and  ${}^{11}_\Lambda\text{Be}$  spectroscopy


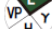










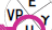








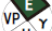




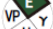
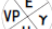



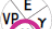



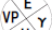



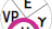



Isomultiplet	${}^4_\Lambda\text{He}-{}^4_\Lambda\text{H}$	${}^7_\Lambda\text{Be}-{}^7_\Lambda\text{Li}^*$	${}^7_\Lambda\text{Li}^*-{}^7_\Lambda\text{He}$	${}^8_\Lambda\text{Be}-{}^8_\Lambda\text{Li}$	${}^9_\Lambda\text{B}-{}^9_\Lambda\text{Li}$	${}^{10}_\Lambda\text{B}-{}^{10}_\Lambda\text{Be}^*$
Shell model (Gal <i>et al.</i> ) [41]	+226	-17	-28	+49	-54	-136
Cluster model (Hiyama <i>et al.</i> ) [39, 40]		+150	+130			+20
No-core shell model (Le <i>et al.</i> ) [43]	+238	-35	-16	+143		
Experiment	$+233 \pm 92$	$-100 \pm 90$	$-20 \pm 230$	$+40 \pm 60$	$-210 \pm 220$	$-220 \pm 250$

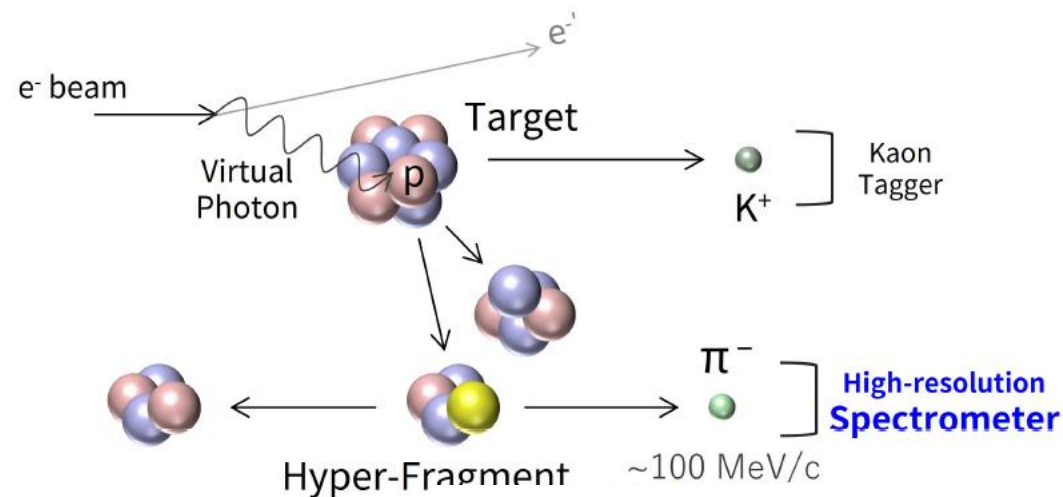
Existing data accuracy is sufficient for CSB study.

$$|\Delta B_\Lambda^{\text{total}}| = \sqrt{(\Delta B_\Lambda^{\text{stat.}})^2 + (\Delta B_\Lambda^{\text{sys.}})^2} \leq \mathbf{70 \text{ keV}}$$

Electron-beam experiment at JLab  Emulsion experiment  
Hadron-beam experiment at J-PARC   $\gamma$ -ray experiment

Hypernucleus		T<0	T=0	T>0	CSB study		
s-shell	$\mathbf{d} \mathbf{N} \mathbf{\Lambda}$ (0 <sup>+</sup> ) (1 <sup>+</sup> )	${}^4_\Lambda\text{H}$ 		${}^4_\Lambda\text{He}$ 	Now 	New JLab 	J-PARC 
		 					
p-shell	$\mathbf{\alpha} \mathbf{N} \mathbf{\Lambda}$	${}^6_\Lambda\text{He}$ 		${}^6_\Lambda\text{Li}$ 			
	$\mathbf{\alpha} \mathbf{N} \mathbf{N} \mathbf{\Lambda}$	${}^7_\Lambda\text{He}$ 	${}^7_\Lambda\text{Li}^*$ 	${}^7_\Lambda\text{Be}$ 			
	$\mathbf{\alpha} \mathbf{d} \mathbf{N} \mathbf{\Lambda}$	${}^8_\Lambda\text{Li}$ 		${}^8_\Lambda\text{Be}$ 			
	$\mathbf{\alpha} \mathbf{d} \mathbf{N} \mathbf{N} \mathbf{\Lambda}$	${}^9_\Lambda\text{Li}$ 	${}^9_\Lambda\text{Be}$ 	${}^9_\Lambda\text{B}$ 			
	$\mathbf{\alpha} \mathbf{\alpha} \mathbf{N} \mathbf{\Lambda}$	${}^{10}_\Lambda\text{Be}$ 		${}^{10}_\Lambda\text{B}$ 			
	$\mathbf{\alpha} \mathbf{\alpha} \mathbf{N} \mathbf{N} \mathbf{\Lambda}$	${}^{11}_\Lambda\text{Be}$ 	${}^{11}_\Lambda\text{B}$ 	${}^{11}_\Lambda\text{C}$ 			
	$\mathbf{\alpha} \mathbf{\alpha} \mathbf{d} \mathbf{N} \mathbf{\Lambda}$	${}^{12}_\Lambda\text{B}$ 		${}^{12}_\Lambda\text{C}$ 			

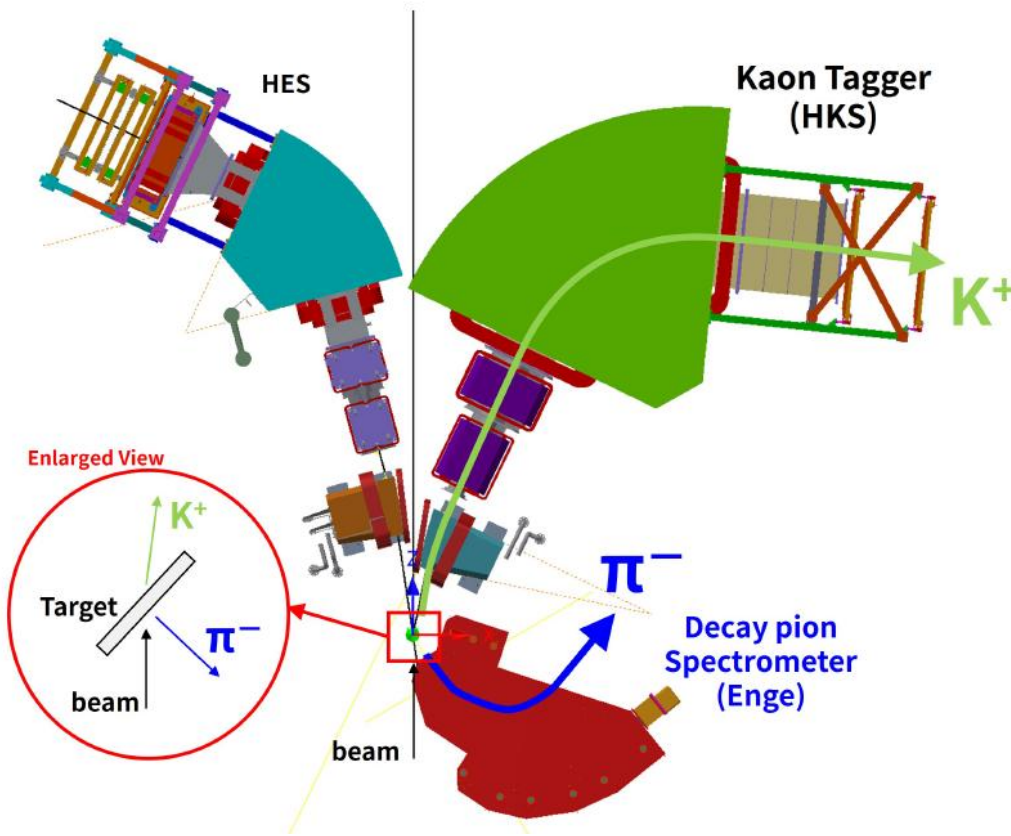
# Run Group Addition E12-20-013A/E12-15-008A

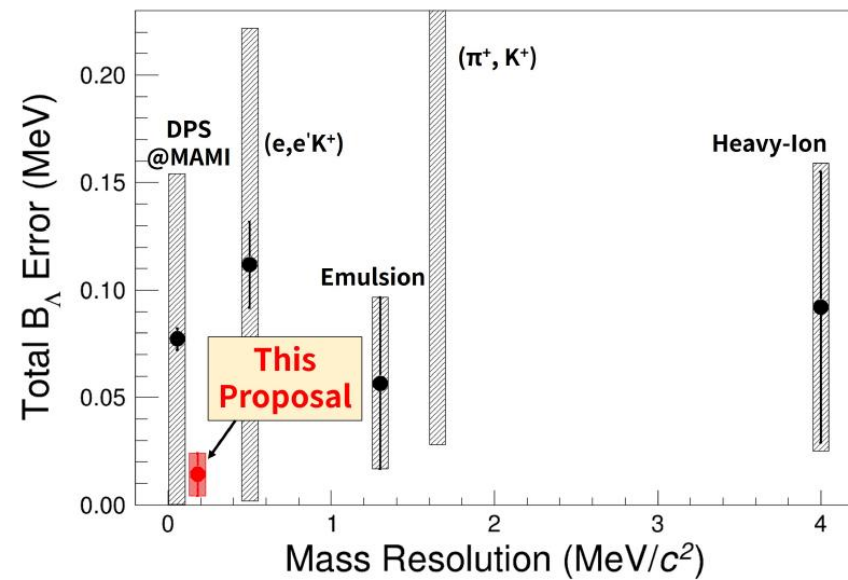


$$B_{\Lambda} = M_{\text{core}} + M_{\Lambda} - M_{HYP}, \quad M_{HYP} = \sqrt{M_{\text{nucl}}^2 + p_{\pi^-}^2} + \sqrt{M_{\pi^-}^2 + p_{\pi^-}^2}.$$

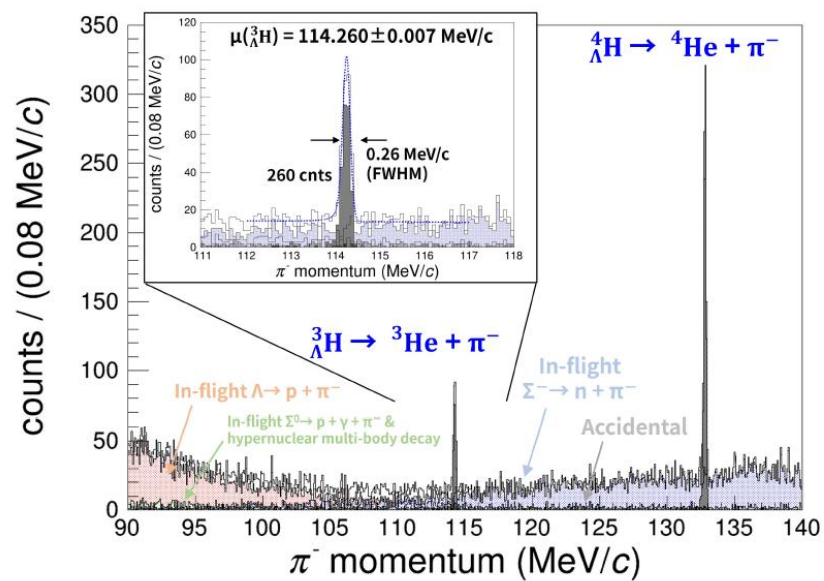
Hypernuclei	Decay mode	$p_{\pi^-}$ (MeV/c)
${}^3_{\Lambda}\text{H}$	${}^3\text{He} + \pi^-$	114.4
${}^4_{\Lambda}\text{H}$	${}^4\text{He} + \pi^-$	133.0
${}^6_{\Lambda}\text{H}$	${}^6\text{He} + \pi^-$	135.3
${}^7_{\Lambda}\text{He}$	${}^7\text{Li} + \pi^-$	115.1
${}^7_{\Lambda}\text{Li}$	${}^7\text{Be} + \pi^-$	108.1
${}^8_{\Lambda}\text{He}$	${}^8\text{Li} + \pi^-$	116.5
${}^8_{\Lambda}\text{Li}$	${}^8\text{Be} + \pi^-$	124.2
${}^8_{\Lambda}\text{Be}$	${}^8\text{B} + \pi^-$	97.2
${}^9_{\Lambda}\text{Li}$	${}^9\text{Be} + \pi^-$	121.3
${}^9_{\Lambda}\text{B}$	${}^9\text{C} + \pi^-$	96.8
${}^{10}_{\Lambda}\text{B}$	${}^{10}\text{C} + \pi^-$	100.5
${}^{11}_{\Lambda}\text{B}$	${}^{11}\text{C} + \pi^-$	86.5
${}^{12}_{\Lambda}\text{B}$	${}^{12}\text{C} + \pi^-$	115.9

A list of expected pion momenta

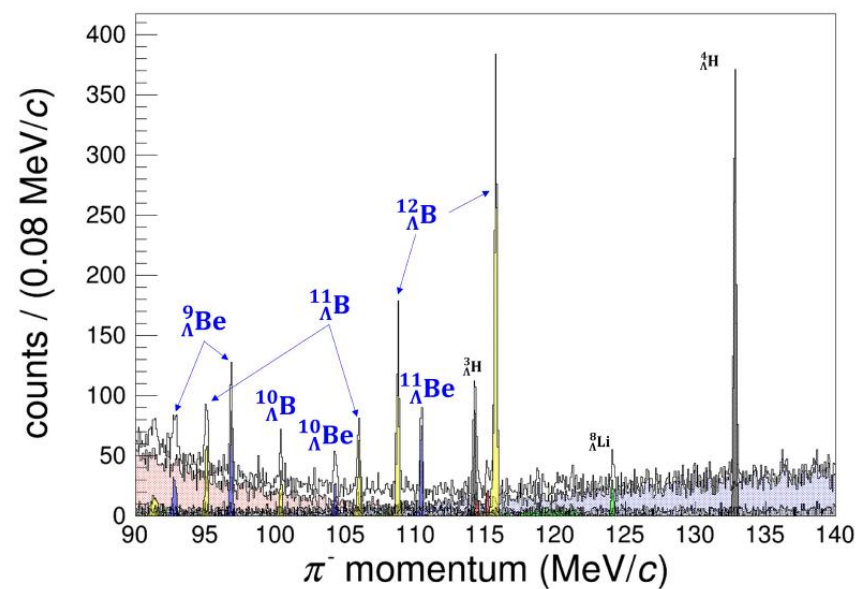




## Pion spectra



Li target



Graphite target

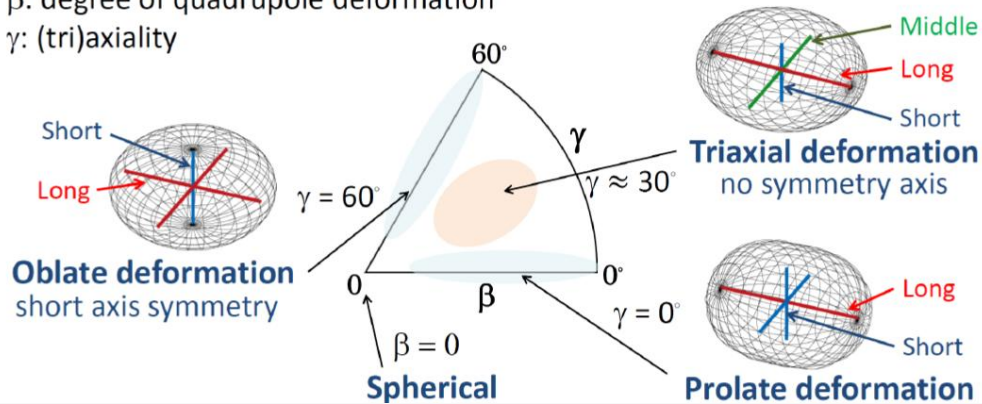
# Study on the nucleus deformations

## (Experiment E12-24-011)

### Parameters to describe deformation

#### Nuclear quadrupole deformation ( $\beta, \gamma$ )

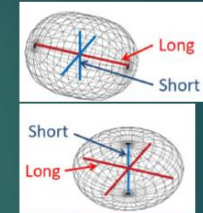
- $\beta$ : degree of quadrupole deformation
- $\gamma$ : (tri)axiality



$^{26}\text{Mg}$  is interesting candidate for triaxially deformed nucleus

Proton  $Z=12$  Prolate

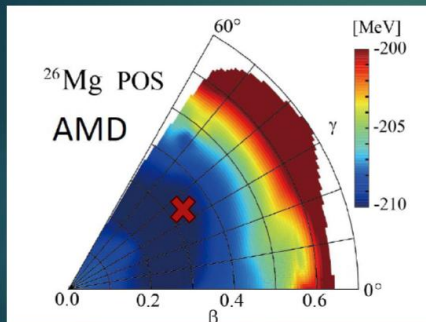
Neutron  $N=14$  Oblate



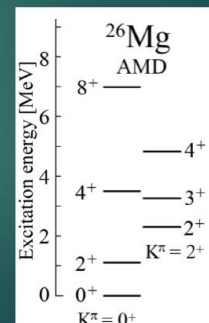
Co-existence of different deformations

Terasaki et al. NPA**621**(1997)  
Rodriguez-Guzman et al. NPA**709** (2002)  
Peru et al PRC**77** (2008)  
Hinohara, Kanada-En'yo PRC**83** (2011)

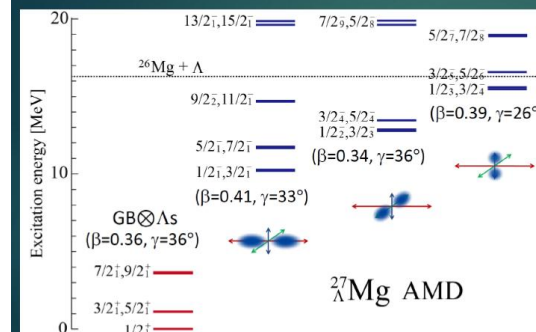
### Recent theoretical calculation



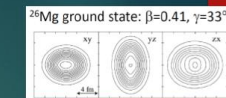
(Hyper)  
Anti-symmetrized Molecular Dynamics  
M. Isaka et al. PRC **83** (2011) 044323.  
PRC **83** (2011) 054304.



### Adding a $\Lambda$ particle



M. Isaka, Hypernuclear Physics Workshop 2023 at JLab

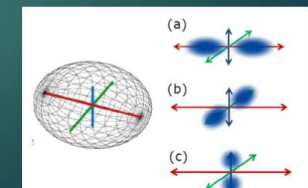


$\Lambda N$  interaction is attractive

WF of  $\Lambda$  in p-orbit is straight

Overlap between  $\Lambda$  and  $^{26}\text{Mg}$  core depends on axis direction

$^{26}\text{Mg} \otimes \Lambda(p)$  splits in 3 states





# Summary

Experiment E12-17-003 is still producing very interesting “byproduct” results:

- a) Measurement of the differential cross section for  $\Lambda/\Sigma^0$  hyperon electroproduction at forward angles, where data are scarce, and at a  $Q^2$  value not well measured so far
- b) **Backward-angle electroproduction of  $\eta'$  mesons off protons at  $W = 2.13$  GeV and  $Q^2 = 0.46$  (GeV/c)<sup>2</sup>**

A very exciting set of experiments will take place in Jlab Hall C aiming to:

- a) Understanding the structure of neutron stars (solving the “hyperon puzzle”).
- b) Studying the Charge Symmetry Breaking (CSB).
- c) Performing measurements of light hypernuclei binding energies with unprecedented precision.
- d) Studying triaxially deformed nuclei.